Phonovoltaic. II. Tuning band gap to optical phonon in graphite

Corey Melnick and Massoud Kaviany

Phonovoltaic: Part II – Tuning bandgap to optical phonon in graphite

Corey Melnick and Massoud Kaviany*

University of Michigan

Department of Mechanical Engineering

Ann Arbor, MI 48105-2125

Abstract

An efficient phonovoltaic (pV) material requires a highly energetic optical phonon ($E_{p,O} \gg k_B T$) with linewidth dominated by the electron-phonon (e-p) coupling and resonant with its electronic bandgap ($\Delta E_{e,g}$), as discussed in Part I (this issue). No current material combines these properties. While graphite (graphene) has the former two, it lacks a bandgap. Opening and tuning the bandgap in graphite is challenging, due to the stability of the Dirac-point, e.g., under a uniaxial strain < 0.25. We tune its bandgap through partial hydrogenation using extensive *ab intio* calculations and find a stable graphame structure with $\Delta E_{e,g} \simeq E_{p,O} \simeq 200$ meV, $C_{128}H_{1\times24}$. We calculate the e-p coupling in tuned $C_{128}H_{1\times24}$ and graphene and show that the transition from π-π^* (graphane) to σ-σ^* (graphame) bands suppresses the electron-phonon coupling, such that optical phonons in $C_{128}H_{1\times24}$ primarily downconvert, and it does not achieve a high figure of merit ($Z_{pV} < 0.1$). *Ab initio* phonon-phonon couplings are calculated for graphane and graphene to support this result. Overall, we develop a material with $E_{p,O} \simeq \Delta E_{e,g} \gg k_B T$ and a method for tuning and evaluating pV materials.

I. INTRODUCTION

Part I[1] (this issue) proposes the phonovoltaic (pV) cell shown in Fig. 1, which harvests nonequilibrium (hot) optical phonons across a bandgap resonant with or smaller than the optical phonon energy. The degree of local nonequilibrium (η_C), the fraction of hot optical phonons which generate an electron rather than downconvert, ($\dot{\gamma}^*_{e-p}$), and the fraction of phonon energy ($E_{p,O}$) preserved by the bandgap ($\Delta E_{e,g}$) limit the pV efficiency. Part I proposes that the figure of merit (Z_{pV}) and efficiency η_{pV} are

$$Z_{pV} = \dot{\gamma}^*_{e-p} \frac{\Delta E_{e,g}}{E_{p,O}} \leq 1, \quad \dot{\gamma}^*_{e-p} = \frac{\dot{\gamma}_{e-p}}{\dot{\gamma}_{e-p} + \dot{\gamma}_{p-p}}, \quad \eta_{pV} \simeq \eta_C Z_{pV}[1 - 0.75 \exp(-\eta_C \frac{\Delta E_{e,g}}{k_B T_c})], \quad (1)$$

where η_C is the Carnot limit given by the local electron-phonon (e-p) nonequilibrium, i.e., $\eta_C = 1 - T_{p,O}/T_c$, and $\dot{\gamma}_{e-p}$ and $\dot{\gamma}_{p-p}$ are the e-p and phonon-phonon (p-p) interaction rates, T_c is the cold, contact temperature, $T_{p,O}$ is the hot optical phonon temperature, and k_B is the Boltzmann constant. Thus, the pV requires $E_{p,O} > \Delta E_{e,g} \gg k_B T$ and that the optical phonon mode has a linewidth dominated by the e-p coupling (high $\dot{\gamma}^*_{e-p}$).
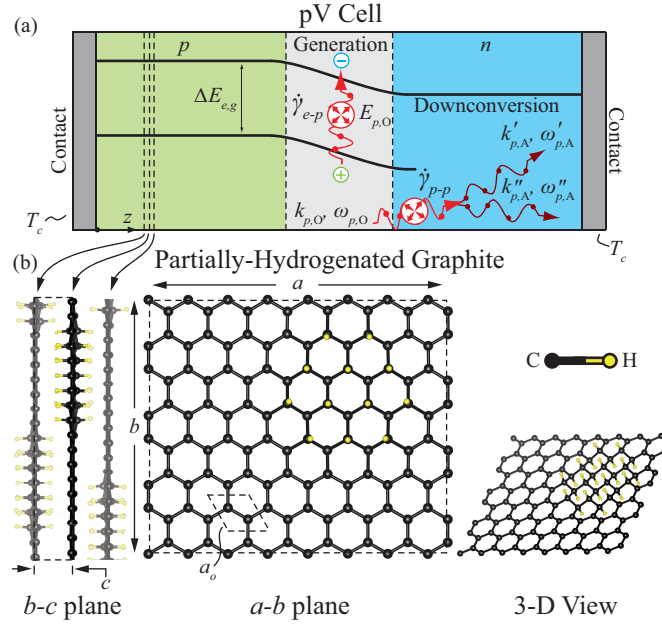

FIG. 1. (a) The function of a phonovoltaic cell comprised of (b) partially-hydrogenated graphite. An excited optical phonon populations creates electron-hole pairs, and the p-n junction separates them to generate power. The hot optical phonons also downconvert into acoustic phonons and generate entropy. Hydrogenation opens a bandgap by transforming the sp^2 hybridized graphene into sp^3 hybridized graphane.

Few semiconductors exist with an optical phonon mode more energetic than the bandgap, and even fewer of these exhibit an optical phonon significantly more energetic than the thermal energy ($k_B T_c$) at room temperature. Energetic phonons require strong bonds between light atoms; however, strong bonding localizes electrons and induces a large bandgap. Indeed, in an isotropic semiconductor strong bonding typically produces a bandgap more than an order of magnitude larger than the optical phonon energy. For example, the strong σ-bonds in diamond produce extremely energetic optical phonon modes (164 meV) and a bandgap exceeding 5 eV. Conversely, the weak bonds in semi-metallic $Hg_{1-x}Cd_xTe$ (MCT) produce a narrow bandgap ($0 \leq \Delta E_{e,g} \leq 1$ eV), but no optical phonon more energetic than 45 meV[2]).

Anisotropic structures enable deviation from this trend through an alternate bonding mechanism, e.g., π- rather than σ-bonding. For example, graphene has a unique combination of electronic and phononic properties due to its sp^2 hybridized structure, wherein π and π^*-bands form near the Fermi surface. Due to the symmetry of graphene, these bands become degenerate at the Dirac-point (K)[3,4].

While the active optical phonon modes in graphene have a linewidth dominated by the e-p coupling ($\dot{\gamma}^*_{e-p} > 0.9$)[5], the lack of a bandgap ensures $Z_{pV} = 0$. If tuning the bandgap of graphite to its optical phonon energy preserved the e-p and p-p coupling properties, then the pV figure of merit would exceed 0.8, and its efficiency would greatly exceed that of a thermoelectric generator.

The alternate group IV 2-D crystal silicene has similarly favorable properties[6], and the bandgap in silicene has been successfully tuned[7]. However, the energy of the optical phonon modes are limited in crystals comprised of second row and higher elements (due to their weight and weaker bonding). Thus, the optical phonon modes in silicene are limited to around 70 meV, and we focus on graphite.

In this study we tune the bandgap of graphite through its partial-hydrogenation. The *ab initio* bandgap is found for partially-hydrognated graphene cells with variations in the atomic fraction and configuration of hydrogen. A stable structure is found which tunes the bandgap to roughly the E_{2g} graphene phonon mode (200 meV). Additional tuning to the E_g graphane mode is accomplished through the application of a small, isotropic strain. Then, the phonon and e-p properties are calculated, and compared with the e-p and p-p coupling in graphene and graphane. The transition from π to σ-type bands is shown to inhibit the

3

e-p coupling and limit the $Z_{\mathrm{pV}} < 0.1$. Finally, additional avenues of research are suggested in the search for an efficient pV material.

II.   TUNING BANDGAP OF GRAPHITE

Opening a bandgap in graphene has attracted substantial attention after its initial discovery. Many methods of achieving this goal have been proposed, e.g., functionalization[8], growth on an ordered substrate[9], and the application of a mechanical strain[10–12], electric field[13] or magnetic field,[14] or through chemical doping[15]. Of these methods, functionalization is chosen for this study. Relying on a substrate to tune the bandgap restricts the pV to a 2-D device. Using electric and magnetic fields in a pV prevents its application in, e.g., electronics cooling, where electromagnetic fields disrupt the electronic packages. Chemical doping can substantially shift the Fermi-level and preclude its use as a diode. Using strain is more attractive, due to the ease with which the strain may be adjusted. However, the Dirac-point in graphene is highly stable, and strain induced bandgap tuning is impractical.

That is, despite the initial *ab initio* results by Ni *et al.* suggesting that arbitrary unixial strains open a bandgap in graphene[16], the tight-binding modeling of Perier *et al.* showed that strains in excess of 0.2 are required to open a bandgap, and they hypothesized that that the *ab intio* simulations missed the movement of the Dirac-point from the K to M point under strain[10]. This supposition was confirmed by Ni *et al.*, who additionally proposed that under the strain requirements proposed by Periera *et al.*, the σ^*-band becomes the lowest-energy conduction band at M and may prevent the a bandgap from opening[17].

Figure 2 presents the *ab initio*[18] low-energy bandstructure for variations in the uniaxial strain. It shows that strains exceeding 0.25 are required to open a gap. While the σ^*-band does cross over the π^*-band to become the first-conduction band, a bandgap still opens at M. However, even under strains exceeding 0.3, the bandgap remains extremely narrow, in part due to the crossing of σ^* and π^*-bands. Such substantial strains are impractical, at best, and fall well beyond the elastic deformation of graphene. Moreover, the application of a tensile strain reduces the energy of the optical phonon modes[19], further limiting strained graphene as a pV material.

In contrast, it has been shown that non-uniaxial strains induce a gauge field which in turn opens a bandgap through the quantum hall effect[11]. However, this approach limits
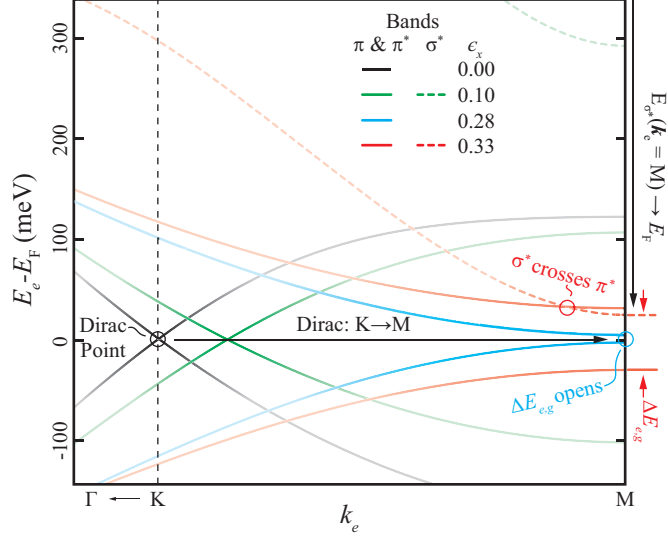
FIG. 2. The low-energy bandstructure of graphene for variations in the uniaxial strain (ϵ_x). Under a small strain, the Dirac-point moves from K towards M and the σ band moves towards the Fermi level at M. Around $\epsilon_x = 0.25$, the Dirac-point reaches M and a bandgap opens between the π bands. Around $\epsilon_x = 0.3$, the σ^* band becomes the first conduction band, reducing the bandgap.

the pV to a 2-D device, whereas functionalization is potentially applicable to graphite and enables a 3-D cell. Thus, this study focuses on functionalization, and in particular, the partial hydrogenation of graphite.

III. PARTIALLY-HYDROGENATED GRAPHITE

Theoretical investigations of graphane (fully-hydrogenated graphene) began before that of graphene[20]. Two stable conformations were discovered, the most stable of which is the chair conformation [Fig. 3(a)], wherein the hydrogen atoms alternately bind above and below carbon atoms in the graphene plane[21]. During hydrogenation, out-of-plane hydrogen atoms transform the local, sp^2 hybridized graphene structure into a sp^3 hybridized graphane structure. The resulting planar sp^3 structure localizes electrons within the σ-bond and opens a bandgap. Theoretical studies predicted a bandgap as high as 3.5-3.7 eV in graphane, depending on the conformation[22]. Although full hydrogen coverage has not been achieved experimentally, experimental and reversible hydrogenation of graphene has provided evidence for graphane[23] and its phonon properties, which are supported theoretically[24].

As the structural stability of graphame (partially-hydrogenated graphene) increases with hydrogen coverage, it is predicted that islands of hydrogenated carbon forms in a particular

conformation and that these islands expand as hydrogenation continues[20,22]. An example of such an island is shown in Fig. 3(d). As the hydrogenation progresses, the bandgap opens until full coverage is achieved. Thus, the bandgap of graphite is tuned by controlling the extent of the hydrogenation.
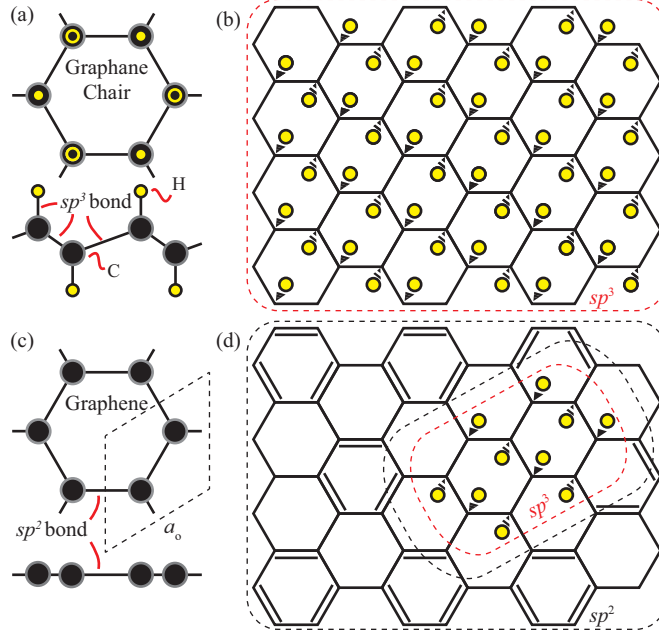

FIG. 3. (a,b) Graphane in the chair configuration and (c) graphene and (d) partially hydrogenated graphene. Hydrogenation opens a bandgap by altering the sp^2 hybridized structure of graphene and transforming it into a sp^3 structure.

For the *ab initio* calculations to follow, the initial configuration chosen for the simulations within the density functional theory (DFT) and the density functional perturbation theory (DFPT) have a substantial impact on the resulting predictions. Thus, constructing a graphame supercell requires care. Indeed, the location of added hydrogen atoms, their conformation, and the number of hydrogen atoms compared to the number of carbon atoms all influence the resulting electronic and phononic properties.

The pV cell requires a non-negligible volume to generate substantial current and power[1]. Thus, a practical pV cell requires the 3-D structure of partially hydrogenated graphite rather than the Angstrom thickness, 2-D structure of graphame. However, accurate *ab initio* simulation of partially hydrogenated graphite offers a significant challenge. Restricting the simulations to 2-D structures (graphame) significantly reduces the computational demand and number of structural variants. Fortunately, as the in-plane bonds dominate the cross-plane van der Waals interactions, the graphame simulations accurately approximate the

electronic and phononic properties of partially-hydrogenated graphite.[25] Thus, this study is restricted to the simulation of graphame.
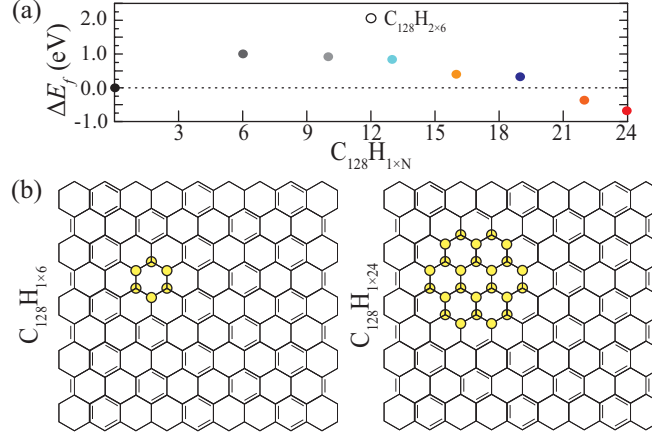

FIG. 4. (a) Formation energy of graphame structures for an increasing number of hydrogen in a chair configured island. Each island tested has fully hydrogenated carbon rings ($C_6H_{1\times6}$). Nearly complete concentric rings (22 H) or complete concentric rings (24 H) are required for stability. (b) Graphame cells $C_{128}H_{1\times6}$ and $C_{128}H_{1\times24}$ are shown.

A rectangular graphene supercell of 128 carbon atoms (C_{128}) forms the scaffolding for the simulated graphame cells. Hydrogen atoms are placed onto this scaffold in the chair configuration in fully-hydrogenated rings ($C_{128}H_{1\times6}$), as these are expected be more stable than a partially-hydrogenated carbon ring. Structures involving multiple rings ($C_{128}H_{N_R\times6}$) and larger hydrogenated islands are tested $C_{128}H_{1\times N_H}$, where N_R and N_H are the number of rings and atoms. For example, two or three conjoined rings create a 10 H island ($C_{128}H_{1\times10}$) or 13 H island ($C_{128}H_{1\times13}$). $C_{128}H_{1\times6}$ and $C_{128}H_{1\times24}$ are shown in Fig. 4(b). These structures are relaxed within DFT[26], and their formation energies are shown in Fig. 4(a).

While a single hydrogen ring ($C_{128}H_{1\times6}$) is unstable, further and adjacent hydrogenation increases stability (while additional, non-adjacent rings do not). Thus, it remains likely that islands of hydrogen form and then expand outward. These results additionally suggest that the hydrogen prefers to form in even-numbered clumps such that all electrons pair. As expected, stability increases as the internal sp^3 structure grows larger than the strained sp^3-sp^2 interface at the graphene-graphane border.
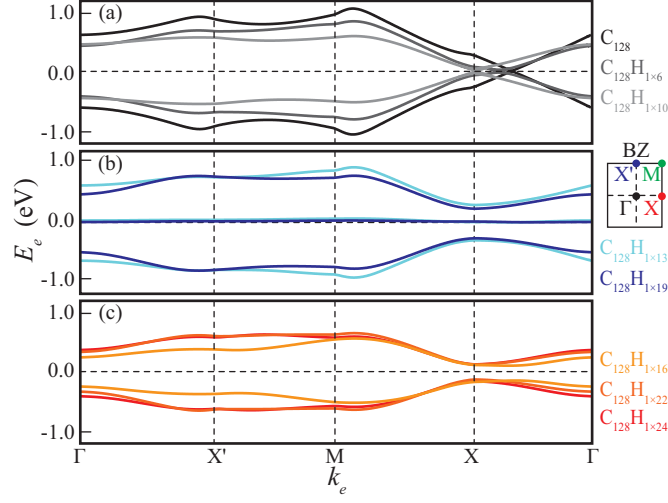
7

FIG. 5. Electron Dispersion of lowest-energy bands in graphene (C_{128}) and graphame ($C_{128}H_{N_R \times N_H}$) for variation in the number of islands (N_R) and number of hydrogen atoms per island (N_H). (a) At low hydrogen concentrations, no bandgap opens but the Dirac-point moves towards X along the Γ-X high-symmetry line. (b) A trap band forms for an uneven number of hydrogen atoms. (c) At large hydrogen concentrations, however, a narrow bandgap opens at X. Some discontinuities arise from the crossing of the π and σ bands.
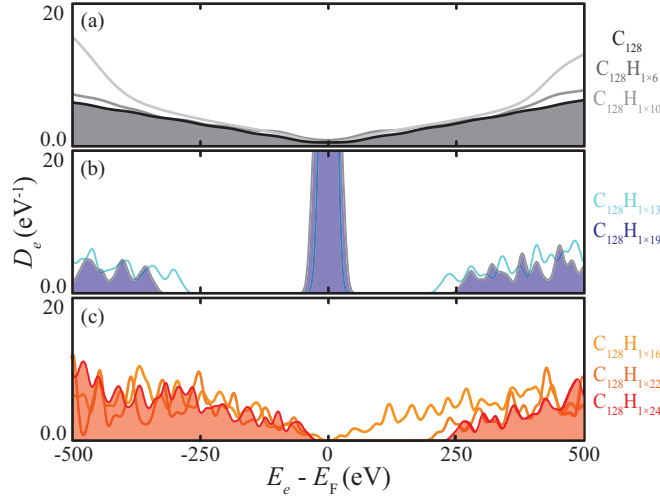

FIG. 6. Electron density of states for graphene and graphame. The density of states is not affected significantly at (a) low hydrogen concentrations, (b) unless an unpaired electron is left in the structure ($C_{128}H_{1\times13}$, $C_{128}H_{1\times19}$). (c) A significant bandgap is not formed until the structures become stable ($C_{128}H_{1\times22}$), at which point a 250 meV bandgap opens.

IV. ELECTRON PROPERTIES

The *ab initio* electronic properties of graphame are presented in Figs. 5 and 6[27] for a small (a), odd (b), and large (c) number of H atoms. When a small and even number of hydrogen

are present, no bandgap opens, but the Dirac-point moves along the Γ-X line towards X. Only after the hydrogen island occupies a substantial portion of the graphame unit cell does a bandgap open (at X), and this bandgap exceeds 200 meV, i.e., the most energetic phonon mode in graphite. When an odd number of hydrogen are present, the un-paired electron is trapped at the Fermi surface with a substantial energy gap between this trapping band and the valence and conduction bands.

These results, in addition to the substantial strains required to open a bandgap (see Section II), demonstrates the stability of the Dirac-point, which has been linked to translation and time invariance (i.e., its symmetry)[28]. This presents a challenge when tuning the bandgap to resonate with the optical phonons. However, once sufficient hydrogenation opens a bandgap and shifts the topology, arbitrary perturbations tune the bandgap.

Indeed, the bandgap becomes highly sensitive to the lattice constant (i.e., isotropic strains or thermal expansion) and the addition of additional hydrogen atoms. For example, the bandgap in $C_{128}H_{1\times24}$ changes from a 250 to a 175 meV bandgap under a isotropic strain of -0.02, while the bandgap of $C_{128}H_{1\times24}$ is 15 meV larger than $C_{128}H_{1\times22}$. Fine-tuning the bandgap of graphame through hydrogenation in *ab initio* simulation is challenging, as large structures (e.g., $C_{512}H_{2\times16,2\times22}$) are required to achieve $\Delta E_{e,g} \simeq E_{p,O}$. Evaluating the phonon and *e-p* properties in a 600 atom cell is computationally impractical. Thus, this study utilizes small and isotropic strains to fine-tune the bandgap of $C_{128}H_{1\times24}$ to resonate with the desired optical phonon mode.

V.   PHONON PROPERTIES

The phonon hamiltonian discussed in part I[1] is[29,30],

$$\langle \varphi \rangle = \langle \varphi \rangle_{\circ} + \frac{1}{2!} \sum_{ijxy} \Gamma_{ij}^{xy} d_i^x d_j^y + \frac{1}{3!} \sum_{ijkxyz} \Psi_{ijk}^{xyz} d_i^x d_j^y d_k^z + ..., \tag{2}$$

where $\langle \varphi_o \rangle$ is the potential at equilibrium, d_i^x is the displacement of atom i from equilibrium in the x-direction (Cartesian), and Γ and Ψ are the second (harmonic) and third-order (anharmonic) force constants. The harmonic interactions form the dynamical matrix which determines the phonon frequencies $\omega_{k_p,\alpha}$ and displacement vector $\epsilon_{k_p,\alpha}$ for a phonon with

9

polarization α at wavevector $\boldsymbol{k}_p$, where the dynamical matrix is

$$D_{ij}^{xy}(\boldsymbol{k}_p) = \frac{1}{(m_i m_j)^{1/2}} \Gamma_{ij}^{xy} \exp[\imath \boldsymbol{k}_p \cdot (\boldsymbol{r}_i - \boldsymbol{r}_j)], \tag{3}$$

and $\boldsymbol{r}_i$ and m_i are the position and mass of atom i, and its eigenvalues and eigenvectors are $\omega_{\boldsymbol{k}_p,\alpha}^2$ and $\boldsymbol{\epsilon}_{\boldsymbol{k}_p,\alpha}$. The amplitude of the resulting atomic displacement for atom i is

$$u_{\boldsymbol{k}_p,\alpha}^i = \left(\frac{\hbar}{2m_i \omega_{\boldsymbol{k}_p,\alpha}}\right)^{1/2}. \tag{4}$$

In comparison, the anharmonic forces are responsible for the p-p interactions, e.g., the upconversion of two acoustic phonons into an optical phonon and the downconversion of an optical phonon into two acoustic phonons (hereafter referred to as up- and downconversion). These are evaluated for graphene and graphane zone-center phonons in Section VI.B.

The ab $initio$ dynamical matrices are evaluated within DFPT[31] on a rough mesh of k_p points[32]. These dynamical matrices are Fourier transformed into real-space and then interpolated to an arbitrary point in k_p space. The resulting phonon dispersion and density of states for graphene, graphane, and $C_{128}H_{1\times24}$ are shown in Fig. 7.

The active optical phonon modes in graphene are the E_{2g} and A_1' modes, where the A_1' mode is at a Kohn anomoly and couples most strongly to the electronic system. The hydrogenation of graphene substantially changes the phonon properties. Graphane exhibits an extremely energetic optical phonon mode per Hydrogen atom: The out-of-plane vibration of hydrogen, as well as the less energetic E_g (rather than E_{2g}) mode. Moreover, the optical modes in graphane tend to have lower group velocities. Graphame exhibits a mix of these modes, some smeared and distorted by the graphene-graphane border.

VI.   E-P AND P-P COUPLING

As discussed in Part I[1], the relaxation of hot optical phonons through the generation of new electrons or acoustic phonons largely determines the performance of a pV cell. The e-p and anharmonic p-p couplings drive these phenomena. This section presents the ab $initio$ coupling and kinetics from perturbation theory for both coupling mechanisms.
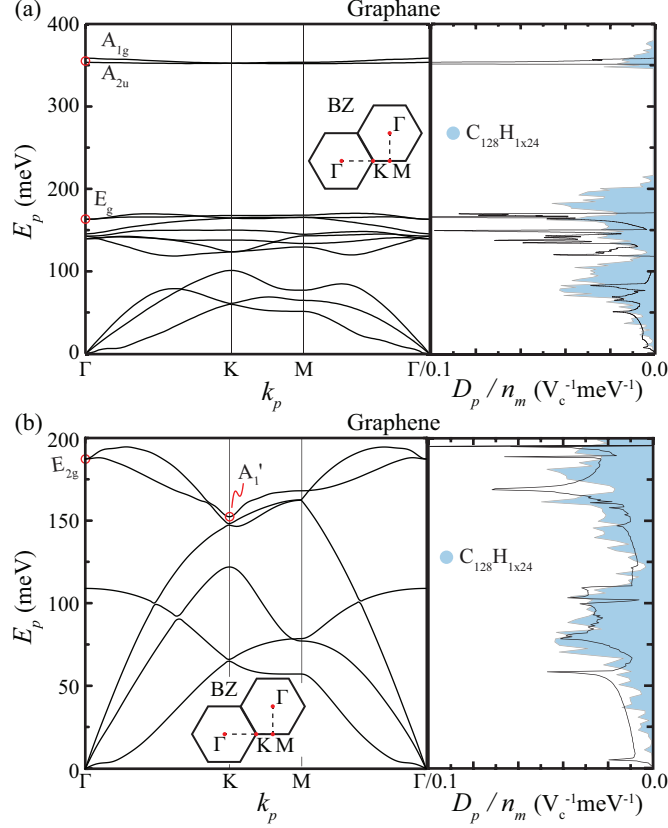
FIG. 7. Phonon dispersion and density of states (D_p) for (a) graphane, (b) graphene, and $C_{128}H_{1\times24}$, where D_p is scaled by the number of modes (n_m) per unit cell. As expected, the $C_{128}H_{1\times24}$ phonon density of states shows a combination of the graphene and graphane optical phonon modes. These include (in order of energy) the energetic A_{1g} and A_{2u} graphane modes (out-of-plane hydrogen vibration), the E_{2g} mode (graphene), the A_1' mode (graphene mode - Kohn Anomaly), and E_g (graphane).

A. *e-p* coupling and kinetics

The *e-p* hamiltonian is presented in Part I[1], and a brief description of the resulting *e-p* matrix element follows. When a phonon with momentum $\boldsymbol{k}_p$ and polarization α scatters with an electron of momentum $\boldsymbol{k}_e$ in band i ($|\boldsymbol{k}_e i\rangle$), it annihilates that electron and creates an electron in band j with momentum $\boldsymbol{k}'_e$ ($|\boldsymbol{k}'_e i\rangle$). The *e-p* coupling element $M_{\boldsymbol{k}_e i,\boldsymbol{k}'_e j,\alpha}$ which follows from this hamiltonian is

$$M_{\boldsymbol{k}_e i,\boldsymbol{k}'_e j,\alpha} = \langle \boldsymbol{k}_e, i| \frac{\partial \varphi_{\text{KS}}}{\partial u_{\boldsymbol{k}_p,\alpha}} |\boldsymbol{k}'_e, j\rangle \left(\frac{\hbar}{2\langle m\rangle \omega_{\boldsymbol{k}_p,\alpha}} \right)^{1/2} \delta_{\boldsymbol{k}_e,\boldsymbol{k}'_e \pm \boldsymbol{k}_p}, \tag{5}$$

where φ_{KS} is the Kohn-Sham potential[31]. The δ-function conserves momentum during phonon absorption (+) and emission (−), such that $\boldsymbol{k}'_e = \boldsymbol{k}_e \pm \boldsymbol{k}_p$.

11

The interaction rate follows from the Fermi golden rule[29]

$$\dot{\gamma}_{e-p}(\boldsymbol{k}_p, \alpha) = \frac{1}{\boldsymbol{k}_e} \sum_{\boldsymbol{k}_e, i, j} \frac{2\pi}{\hbar} |M_{\boldsymbol{k}_e i, \boldsymbol{k}'_e j, \alpha}|^2 \delta(E_e \pm \hbar\omega_{\boldsymbol{k}_p, \alpha} - E'_e)[f_e(E_e) - f_e(E_e \pm E'_e)], \quad (6)$$

where the δ-function conserves energy such that $E'_e = E_e \pm \hbar\omega_{\boldsymbol{k}_p, \alpha}$, and $f_e(E_e)$ is the electron occupancy at energy E_e.

Typically, the Fermi-Dirac occupancy applies, i.e.,

$$f_e = [\exp(\frac{E_e - E_{\mathrm{F}}}{k_{\mathrm{B}}T}) + 1]^{-1}, \quad (7)$$

where E_{F} is the Fermi energy and T is the temperature. When $\Delta E_{e,g} \gg k_{\mathrm{B}}T$, the electron occupancy in valence states approaches unity, and the occupancy in conduction states vanishes. This greatly inhibits the e-p interaction rate between two valence ($f_e \simeq f'_e$) or conduction ($f_e \simeq 0$) states. Thus, when $E_{p,\mathrm{O}} > \Delta E_{e,g}$, this ensures that the valence-to-conduction transitions (i.e., generation and recombination events) dominate the valence-to-valence and conduction-to-conduction transitions. Thus, the summation over i and j is restricted to generation events, i.e., $i = v$ and $j = c$, and the remaining interactions are neglected.

The interaction elements for the Γ-point phonon modes in a $C_{128}H_{1\times24}$ cell are evaluated within DFPT using Quantum Espresso on a $6 \times 6 \times 1$ k_e mesh, wherein the matrix elements are calculated as

$$|M_{\boldsymbol{k}_e v, \boldsymbol{k}_e c, \alpha}|^2 = \sum_{ij, xy} u_{\Gamma, \alpha}^{xi} M_{xi}^* M_{yj} u_{\Gamma, \alpha}^{yj}, \quad (8)$$

where * denotes the complex conjugate, $u_{\Gamma, \alpha}^{xi} = (u\epsilon)_{\Gamma, \alpha}^{xi}$, and M_{xi} is the e-p matrix element associated with a perturbation on atom i in direction x, i.e.,

$$M_{xi} = \langle \boldsymbol{k}_e, v | \frac{\partial \varphi_{\mathrm{KS}}}{\partial x_i} | \boldsymbol{k}_e, c \rangle. \quad (9)$$

These elements, along with the ground state conduction and valence energy surfaces are interpolated onto a $2000 \times 2000 \times 1$ k_e mesh in the first BZ. This fine k_e mesh enables an accurate calculation of Eq. (6) using a Lagrangian δ-function with 1 meV of smearing.

Figure 8 shows the e-p coupling between the lowest conduction and highest valence bands
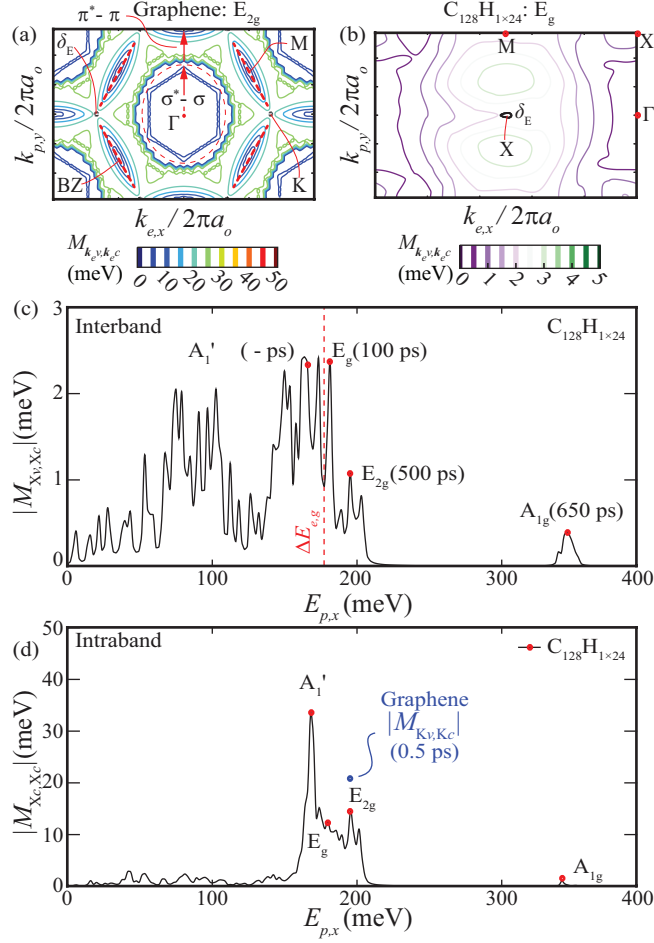
12

FIG. 8. Contours of constant e-p coupling ($|M_{e-p}|$) and energy conserving lines (δ_E) of a selected phonon modes in (a) graphene and (b) $C_{128}H_{1\times24}$. The (c) intraband and (d) interband e-p coupling strength at the band-edge (X) for variations in $E_{p,O}$ and the phonon lifetime ($1/\dot{\gamma}_{e-p}$) of selected modes.

in (a) graphene for the E_{2g} and (b) $C_{128}H_{1\times24}$ for the E_g optical phonon modes. After hydrogenation, the interband e-p coupling is substantially reduced near the band-edge. Indeed, Fig. 8(c) shows the weak interband coupling in graphame for all optical phonon modes at the bandedge (X), and that the e-p lifetime increases from 0.5 ps in graphene to over 100 ps in graphame. However, the intraband coupling elements shown in Fig. 8(d) are not substantially weakened by the hydrogenation.

The poor overlap between σ and σ^* bands explains these results. Note that near the Γ-point in graphene, the σ-bands are nearest the Fermi surface, and Fig. 8(a) shows the weak coupling in this region. In comparison, the π-π^* band coupling near K and M is strong, as these bands overlap significantly.

13

Hydrogenation opens a bandgap by transforming graphene from a sp^2 to sp^3 hybridized structure. During this transition, the σ bands approach the Fermi surface and replace the π bands as the lowest energy bands. At this point, a bandgap opens. As the coupling between the σ-σ^* bands remains weak, so too does the interband coupling in graphame. In contrast, two conduction or valence states overlap completely, such that the intraband coupling remains strong. Thus, the e-p coupling of the E$_{2g}$mode in graphame is reduced from its value in graphene by approximately the atomic hydrogen fraction, rather than an order of magnitude.

A pV material must achieve stronger e-p coupling in order to succeed as a pV material. As functionalized graphene variants often transition from sp^2 to sp^3 hybridization, these materials, like graphame, will not achieve a high figure of merit due to the poor overlap between their σ and σ^* bands. An efficient pV material must achieve stronger e-p coupling, as the anharmonic phonon couplings, in comparison, do not change substantially. This is discussed in the following sections.

B. p-p coupling and kinetics

As discussed in Section V, the anharmonic (third-order and higher) interactions are responsible for phonon downconversion. However, fourth-order and higher interactions are typically masked by the third-order coupling[33]. The rate at which a phonon $(\boldsymbol{k}_p, \alpha)$ downconverts into two phonons $(\boldsymbol{k}'_p, \alpha'$ and $\boldsymbol{k}''_p, \alpha'')$ follows from Eq. (2) and the Fermi golden rule, i.e.,

$$\dot{\gamma}_{p-p}(\boldsymbol{k}_p, \alpha) = \frac{1}{N_k} \frac{\pi \hbar}{16} \sum_{\alpha' \alpha'' \boldsymbol{k}'_p \boldsymbol{k}''_p} |\Psi_{\alpha \alpha' \alpha''}^{\boldsymbol{k}_p \boldsymbol{k}'_p \boldsymbol{k}''_p}|^2 \delta(\omega_{\boldsymbol{k}_p, \alpha} - \omega_{\boldsymbol{k}'_p, \alpha'} - \omega_{\boldsymbol{k}''_p, \alpha''})(f'_p + f''_p + 1), \qquad (10)$$

where f_p is the phonon occupancy, N_k is the number of $\boldsymbol{k}'_p$ points used in the integration[34], and the interaction element $\Psi_{\alpha \alpha' \alpha''}^{\boldsymbol{k}_p \boldsymbol{k}'_p \boldsymbol{k}''_p}$ is

$$\Psi_{\alpha \alpha' \alpha''}^{\boldsymbol{k}_p \boldsymbol{k}'_p \boldsymbol{k}''_p} = \sum_{ijk} \sum_{xyz} \Psi_{ijk}^{xyz} u_{\boldsymbol{k}_p, \alpha}^{xi} u_{\boldsymbol{k}'_p, \alpha''}^{yj} u_{\boldsymbol{k}'_p, \alpha''}^{zk} \delta_{\boldsymbol{k}_p \boldsymbol{k}'_p \boldsymbol{k}''_p}. \qquad (11)$$

For a Γ-point phonon, Eq. (10) is simplified, as momentum conservation dictates $\boldsymbol{k}'_p =$

$-\boldsymbol{k}_p''$, i.e.,

$$\dot{\gamma}_{p-p}(\Gamma,\alpha) = \frac{1}{N_k}\frac{\hbar\pi}{16}\sum_{\alpha'\alpha''\boldsymbol{k}_p'}|\Psi_{\alpha\alpha'\alpha''}^{\Gamma\boldsymbol{k}_p'-\boldsymbol{k}_p'}|^2\delta(\omega_{\Gamma,\alpha} - \omega_{\boldsymbol{k}_p',\alpha'} - \omega_{\boldsymbol{k}_p',\alpha''})(f_p' + f_p'' + 1). \qquad (12)$$

Restricting the calculation to the lifetime of the zone-center phonon modes greatly reduces the number of third-order coupling elements required to evaluate the downconversion rate and simplifies their calculation. As the third-order force constant calculations are computationally costly, this is extremely important, especially in crystals with more than a few atoms per unit cell.

However, evaluating the third-order force constants in $C_{128}H_{1\times24}$ remains unreasonable even under this restriction. Thus, the p-p lifetimes are evaluated from pure graphene and graphane crystals to estimate the lifetimes of the various targeted optical phonon modes. For both of these structures, the third-order force constants are evaluated within DFPT using the $2n+1$ formula[35], as implemented within Quantum Espresso on a $18\times18\times1$ $\boldsymbol{k}_p$ point mesh. These dynamical matrix derivatives are fourier transformed into real space and then interpolated onto a $200\times200\times1$ mesh of $\boldsymbol{k}_p$ points. Then, the integration in Eq. (12) is calculated using a Lagrangian δ-function with 20 K smearing.

Figure 9(a) shows the the downconversion paths for the graphene E_{2g} and graphane E_g phonon modes, (b) the energy of the phonon modes created, and (c) their lifetimes. Due to the high energy of these modes, the phonon lifetimes begin to change significantly around 500 K. Also shown in Fig. 9(c) is the increased downconversion rates of the zone-center optical phonon modes in graphane, as compared to those in graphene. Indeed, even without the degradation of the electron-phonon coupling, hydrogenation enhances the optical phonon downconversion rates and reduces the promising $\dot{\gamma}_{e-p}^*$ of graphene.

C. Figure of merit

Using the results from Sections VI A and VI B, $\dot{\gamma}_{e-p}^*$ is calculated for the zone-center modes in $C_{128}H_{1\times24}$, where $\dot{\gamma}_{e-p}^*$ is

$$\dot{\gamma}_{e-p}^*(\Gamma,\alpha) = \frac{\dot{\gamma}_{e-p}(\Gamma,\alpha)}{\dot{\gamma}_{e-p}(\Gamma,\alpha) + \dot{\gamma}_{p-p}(\Gamma,\alpha)}. \qquad (13)$$
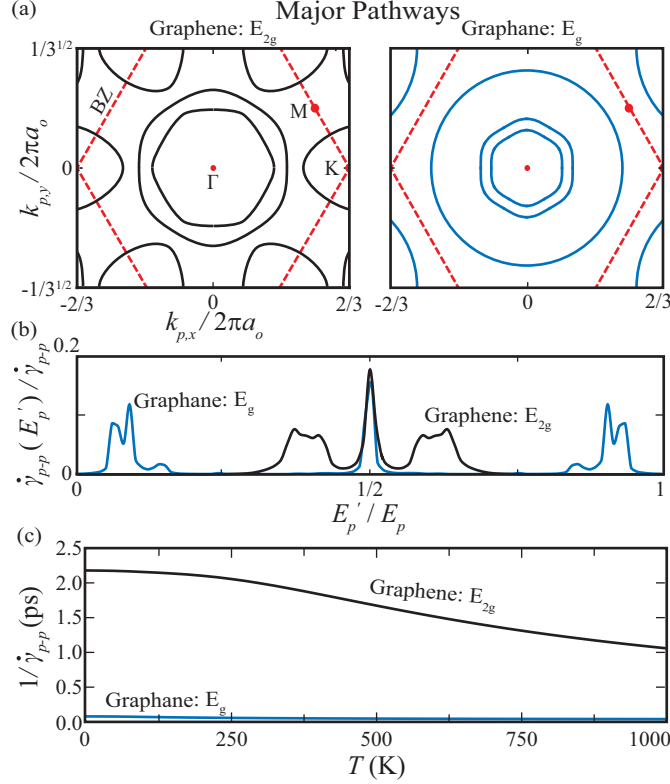
15

FIG. 9. (a) Active downconversion pathways, (b) energy of the phonon modes produced, and (c) the scattering rate as a function of temperature for graphene E_{2g} and graphane E_g modes. Graphane exhibits significantly enhanced optical phonon downconversion rates.

The results are shown in Fig. 10. Note that the $\dot{\gamma}_{p-p}(\Gamma, \alpha)$ used here are from the graphane and graphene calculations.

As shown in Fig. 10, the weak e-p coupling in partially-hydrogenated graphite prevents it from achieving a large $\dot{\gamma}_{e-p}^*$ and Z_{pV}. This weak coupling is due to the small overlap between its valence (σ) and conduction (σ^*) bands. No similar effect reduces the p-p interaction strength, such that the $\dot{\gamma}_{e-p}^*$ achieved by $C_{128}H_{1\times24}$ is less than 0.1. As the bandgap is tuned to resonate with the optical phonon modes, $Z_{pV} = \dot{\gamma}_{e-p}^* < 0.1$.

In graphene, the overlap of π and π^* bands enables a large $\dot{\gamma}_{e-p}^* > 0.9$, but the gapless electronic structure ensures $Z_{pV} = 0$. If the e-p and p-p couplings were to remain unchanged as the bandgap opened, however, graphene would achieve a $Z_{pV} > 0.8$. In such a pV cell, the efficiency significantly exceeds that of a TE, even at room temperature and under negligible e-p nonequilibrium. However, it is challenging to tune the bandgap of graphene without transitioning from π-π^* to σ-σ^* low-energy bands.

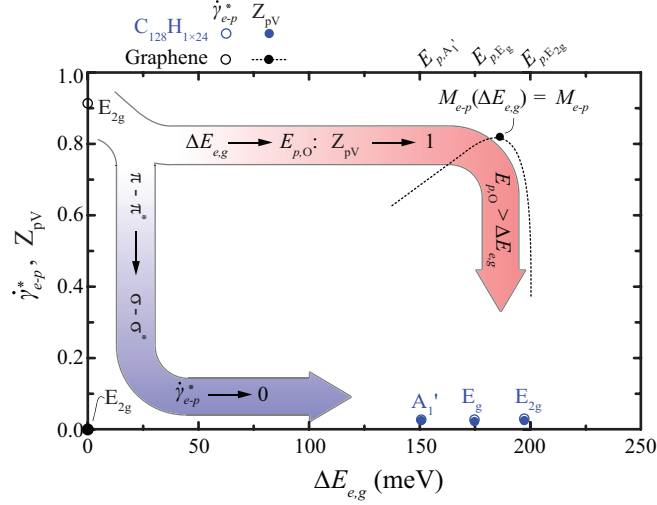For example, hydrogenation, flourination and other functionalization methods which cre-

16

FIG. 10. The fraction of hot optical phonons which generate electrons as they relax ($\dot{\gamma}^*_{e-p}$) and pV figure of merit (Z_{pV}) for graphene and tuned $C_{128}H_{1\times24}$ cells. Also shown is the graphene figure of merit if the e-p and p-p couplings remained constant as the bandgap opens. This figure of merit is substantially larger than that of $C_{128}H_{1\times24}$, as the interaction between the σ and σ^* bands is much weaker than that between the π and π^* bands in Graphene.

ate a sp^3 structure rely on this transition to open a bandgap. If a similar decrease in the interband e-p coupling occurs across all sp^3 hybridized structures, as suspected, few options remain[36]. Thus, it is crucial to confirm this hypothesis. However, other unusual and anisotropic materials may combine the material properties crucial to pV operation: a highly energetic optical phonon mode resonant with the bandgap and with a lifetime dominated by the e-p coupling.

VII.   CONCLUSIONS

In Part I[1], a pV cell is proposed that harvests a hot population of optical phonons resonant with the bandgap and much more energetic than $k_B T$. For efficient harvest, the e-p coupling must dominate the p-p coupling. No current material exists with this combination of properties.

Graphite (graphene), which has energetic optical phonon modes that couple strongly to the electron system, is proposed as a candidate, provided that its bandgap is tuned to the optical phonon energy. Uniaxially strained graphene is confirmed to require extreme strain in order to open a bandgap via a series of *ab initio* calculations, wherein the movement of the Dirac-point along the K-M symmetry line must be carefully tracked. However, the bandgap

17

in graphite may be tuned to its optical phonon modes through its partial-hydrogenation.

Here, this tuning is accomplished through the systematic *ab initio* simulation of partially-hydrogenated graphite layers with variations in the atomic fraction and placement of hydrogen. The $C_{128}H_{1\times24}$ structure is shown to have a bandgap around 250 meV and the arbitrary and isotropic strains enable the fine-tuning to the desired optical phonon mode, e.g., the graphene E_{2g}(200 meV) and the graphane E_g (174 meV) modes.

However, the *e-p* coupling between the σ-σ^* bands in graphane is significantly weaker than the π-π^* band coupling in graphene. In comparison the *p-p* interactions in graphane are similar to or stronger than those in graphene, as shown through the *ab initio* evaluation of graphene and graphene Γ-point phonon lifetimes. Thus, the pV figure of merit for partially-hydrogenated graphite is limited to below 0.1.

The transition of from the π to σ-type bands near the Fermi level as a bandgap opens in graphene due to, e.g., the application of a uniaxial strain or functionalization is proposed to limit alternate graphene derivatives. However, the reduced-dimensioned graphene structures, e.g., quantum-dots and nano-ribbons, preserve the π and π^* bands and may overcome this trend. Additional study remains for other functionalized graphene structures, e.g., flourographane, and a theoretical explanation of the weak σ-σ^* *e-p* coupling is required, and finding alternate pV materials is crucial.

ACKNOWLEDGMENTS

---

[*] kaviany@umich.edu

[1] C. Melnick and M. Kaviany, Phys. Rev. B **x**, x (2015).

[2] A. Rogalski, Rep. Prog. Phys. **68**, 2267 (2005).

[3] S. R. J. Maultzsch, C. Thomsen, H. Requardt, and P. Odejón, Phys. Rev. Lett. **92**, 075501 (2004).

[4] S. Piscanec, M. Lazzeri, F. Mauri, A. Ferrari, and J. Robertson, Phys. Rev. Lett. **93**, 185503 (2004).

[5] N. Bonini, Lazzeri, N. Marzari, and F. Mauri, Phys. Rev. Lett. **99**, 176802 (2007).

[6] J.-A. Yan, R. Stein, and D.M. Schaefer, Phys. Rev. B. **88**, 121403 (2013).

[7] T. P. Kaloni, G. Schreckenbach, and M. S. Freund, J. Phys. Chem. C **118**, 23361 (2014).

[8] V. Georgakilas et al., Chem. Rev. **112**, 6156 (2012).

[9] M. S. Nevius et al., Phys. Rev. Lett. **115**, 13680 (2015).

[10] V. Periera, A. C. Neto, and N. Peres, Phys. Rev. B **80**, 045401 (2009).

[11] F. Guinea, M. Katsnelson, and A. Geim, Nat. Phys. **6**, 30 (2009).

[12] F. M. D. Pellegrino, G. G. N. Angilella, and R. Pucci, Phys. Rev. B **81**, 035411 (2010).

[13] C. Park et al., Phys. Rev. Lett. **115**, 015502 (2015).

[14] M. O. Goerbig, Rev. Mod. Phys. **83**, 1193 (2011).

[15] H. Liu, Y. Liu, and D. Zhu, J. Mater. Chem. **21**, 3335 (2011).

[16] Z. H. Ni et al., ACS Nano **2**, 2301 (2008).

[17] Z. H. Ni et al., ACS Nano **3**, 483 (2009).

[18] The strained graphene unit cells are prepared in Quantum Espresso[37–39] by applying a uniaxial strain on graphene in the x-direction (zig-zag) and then relaxing the cell in the y-direction. Then, a self-consistent DFT simulation on a $120 \times 120 \times 1$ k_e-mesh provides the charge density. The bandstructure is then found along the Γ-K-M high-symmetry line on a $1000 \times 1 \times 1$ k_e-mesh.

[19] T. M. G. Mohiuddin et al., Phys. Rev. B **79**, 205433 (2009).

[20] M. Sluiter and Y. Kawazoe, Phys. Rev. B **68**, 085410 (2003).

[21] M. Pumera and C. Hong, Chem. Soc. Rev. **42**, 5987 (2013).

[22] J. Sofo, A. Chaudhari, and G. Barker, Phys. Rev. B **75**, 153401 (2007).

[23] D. Elias et al., Sci. **30**, 610 (2009).

[24] H. Peelaers, A. Hernández-Nieves, O. Leenaerts, B. Partoens, and F. Peeters, Appl. Phys. Lett. **98**, 051914 (2011).

[25] While the cross-plane transport can not be calculated in graphame simulations, $E_{p,\mathrm{O}}$, $\Delta E_{e,g}$, $\dot{\gamma}_{e-p}$ and $\dot{\gamma}_{p-p}$ can be calculated. It is these properties which largely determine the pV cell operation[1].

[26] The density functional theory code VASP[40–43] with plane-augmented wave[44,45] (PAW) pseudopotentials using the generalized gradient approximation (GGA) and Perdew-Burke-Ernzerof[38,39] functional (PBE) is used to relax the structures to their minimum energy. A k_e mesh of $6 \times 6 \times 1$ and energy cut-off of 400 meV are used until forces converge within 10^{-4} eV/Åand the total energy converges to within 10^{-5} eV, where k_e is the electron wavevector.

[27] The density of states for these structures are calculated on a $30 \times 30 \times 1$ k_e-point mesh.

[28] J. L. Mañes, F. Guinea, and M. A. H. Vozmediano, Phys. Rev. B **75**, 155424 (2007).

[29] M. Kaviany, *Heat transfer physics*, Cambridge University Press, New York, 2nd edition, 2014.

[30] G. Srivistava, *The Physics of Phonons*, Adam Hilger, Bristol, 1990.

[31] S. Baroni, S. de Gironcoli, A. D. Corso, and P. Giannozzi, Rev. Mod. Phys. **73**, 515 (2001).

[32] Graphene and graphane dynamical matrices are calculated on a $18 \times 18 \times 1$ k_p mesh, while only the Γ-point dynamical matrix of $C_{128}H_{1\times24}$ is calculated due to computational constraints. However, this Γ-point calculation contains approximately an $8 \times 8 \times 1$ mesh of atomic force constants.

[33] D. Ecsedy and P. Klemens, Phys. Rev. B **15**, 5957 (1976).

[34] O. Hellman and I. Abrikosov, Phys. Rev. B **67**, 144304 (2003).

[35] X. Gonze and J.-P. Vigneron, Phys. Rev. B **39**, 13120 (1989).

[36] Other options include low-dimension graphene and the noncovalent functionalization of graphene[46].

[37] P. Giannozzi et al., J. of Phys.: Cond. Matter **21**, 395502 (2009).

[38] J. Perdew, K. Burke, and M. Ernzerhof, Phys. Rev. Lett. **77**, 3865 (1996).

[39] J. Perdew, K. Burke, and M. Ernzerhof, Phys. Rev. Lett. **78**, 1396 (1997).

[40] G. Kresse and J. Hafner, Phys. Rev. B **47**, 558 (1993).

[41] G. Kresse and J. Hafner, Phys. Rev. B **49**, 14251 (1994).

[42] G. Kresse and J. Furthmüller, Comput. Mat. Sci. **6**, 15 (1996).

[43] G. Kresse and J. Furthmüller, Phys. Rev. B **54**, 11169 (1969).

[44] P. Blochl, Phys. Rev. B **50**, 17953 (1994).

[45] G. Kresse and D. Joubert, Phys. Rev. B **59**, 1758 (1990).

[46] T. Kuila et al., Prog. in Mat. Sci. **57**, 1061 (2012).